THE JOURNAL OF PHYSICAL CHEMISTRY Letters

pubs.acs.org/JPCL Letter

# Gap-Mode Tip-Enhanced Raman Scattering on Au Nanoplates of Varied Thickness

Rui Wang,[‖] Zhe He,[‖] Alexei V. Sokolov, and Dmitry Kurouski*

Cite This: *J. Phys. Chem. Lett.* 2020, 11, 3815−3820 Read Online

ACCESS | Metrics & More | Article Recommendations | Supporting Information

**ABSTRACT:** Gold nanoplates (AuNPLs) enable the gap-mode configuration of tip-enhanced Raman spectroscopy (TERS). This allows for low-concentration molecular sensing and high-resolution imaging. Compared with non-gap-mode TERS, the gap plasmon provides significantly higher enhancement factors. In addition, AuNPLs exhibit a lightning rod or edge effect, further enhancing the laser field and increasing the spectroscopic sensitivity. In this study, we investigate the relationship between the thickness of AuNPLs and the intensity of the spontaneous Raman signal produced by 4-nitrobenzenethiol, a reporter molecule used in TERS. Our experimental and theoretical results show that the intensity of TERS spectra increases with an increase in the thickness of the AuNPLs. This study of the thickness dependence of AuNPL allows us to find a configuration with maximal nanoplasmonic effects. Moreover, the electromagnetic interaction of the AuNPL with the tip, positioned near the AuNPL's edge, results in a plasmonic nanoantenna configuration for field enhancement, with important promise for future applications to nanobioimaging and biosensing.

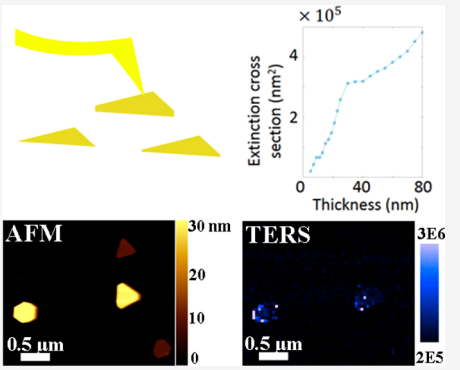




Noble metal nanomaterials (NMNs) are among the most important plasmonic materials due to their broad applicability in various research fields, including bioimaging,[1−3] drug delivery,[4−6] data storage,[7] and catalysis.[8−10] Upon resonant electromagnetic radiation, the collective oscillation of electrons of NMNs can be generated owing to the localized surface plasmon resonance (LSPR) effect.[11−13] As a result, a strong field enhancement can be created in the vicinity of the NMNs. This contributes to the enhancement of Raman scattering of the molecules located in the vicinity of NMNs, with a factor of around $10^6$−$10^9$, a phenomenon known as surface-enhanced Raman spectroscopy (SERS).[14] SERS is a powerful technique used in a variety of applications. However, it does not provide spatial resolution; SERS studies are limited by optical diffraction, similarly to most other far-field spectroscopic techniques. To achieve higher spatial resolution, near-field scanning probe microscopies (SPM), such as scanning tunneling microscopy (STM) and atomic force microscopy (AFM), were developed.[15,16] SPM is capable of providing topological information only, without any insight into its chemical structure. Therefore, it is highly desired to develop a detection method with high spatial resolution while maintaining the high sensitivity feature of SERS.

Tip-enhanced Raman spectroscopy (TERS), a nanospectroscopic technique that combines SPM with LSPR, could provide a solution for the above-mentioned limitations.[17,18] Raman spectra provide unique fingerprints of molecular species, without any labeling or staining required. Besides, TERS enables nanometer or even single-molecule resolution because only molecules in the direct vicinity of the tip will be exposed to the enhanced field and consequently imaged.[19−22] Compared with traditional TERS that provides an enhancement factor of ∼$10^5$, the gap-mode configuration provides a higher enhancement factor of $10^9$,[23−25] which makes it an ideal candidate for investigating analytes on single-molecule[26] and single-monolayer levels.[27−30] The enhancement can be interpreted by recalling that within the tip−substrate gap the electric field is enhanced due to the tip−substrate interaction. Known as the gap-mode plasmon effect, the energy transfer between the tip and AuNPL causes localization of the electric field in the tip−sample junction.[31] Besides, gap-mode plasmon leads to a tighter confinement of the electric field, making the tip a "sharper" probe for single-molecule sensing. In the previous work, the gap-mode configuration has resolved molecular vibrations with angstrom-scale spatial resolution.[21]

In order to improve outcome signals and imaging resolution, we use Au nanoplates (AuNPLs) as TERS substrates in this work. AuNPLs have atomically flat[32] facets exposed as their basal facets,[32,33] making them ideal candidates for the gap-mode TERS substrate. The similar Au nanoplates have been reported efficiently for gap-mode TERS of cystine,[24] nucleic acids,[34] and catalytic processing.[35] The benefits in sensing and

**Received:** March 31, 2020
**Accepted:** April 27, 2020
**Published:** April 27, 2020




https://dx.doi.org/10.1021/acs.jpclett.0c01021
*J. Phys. Chem. Lett.* 2020, 11, 3815−3820

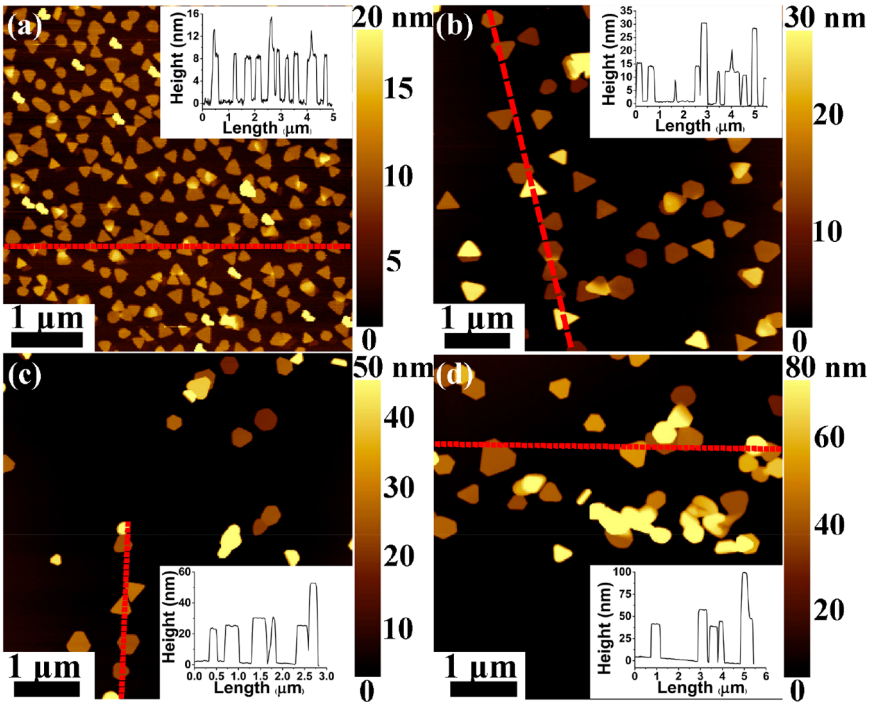


**Figure 1.** (a) AFM images of starting AuNPLs seed with ∼8 nm thickness. AuNPLs underwent isotropic growth with increased thicknesses of (b) ∼15, (c) ∼25, and (d) ∼40 nm. The insets show the corresponding height profiles along the red dashed lines.

photocatalysis raise the significance of studying AuNPL as a substrate. First, AuNPLs are particularly plasmonically active in a spectral range stretching from the visible to the near-infrared, which can overlap with the TERS resonance.[36] In addition, due to their comparable sizes to TERS tips, the tip-AuNPL cavity is supposed to be easily tunable by adjusting cavity parameters, such as the AuNPL thickness. Here we investigate the substrate dependence of gap-mode TERS by fabricating AuNPLs with various thicknesses from 10 to 60 nm. We found that the TERS enhancement was directly correlated with the thickness of AuNPLs, indicating the stronger coupling efficiency of the plasmonic cavity on thicker AuNPLs. This phenomenon was further confirmed by simulations of the tip−AuNPL cavity, which shows a higher absorption/extinction cross section on thicker AuNPLs.

The starting AuNPL seeds were synthesized by a modified seed-mediated growth method that was reported previously,[33,37] followed by isotropic growth[38] to produce AuNPLs with different thicknesses. Figure 1a and Figure S1a show the typical scanning electron microscopy (SEM) and atomic force microscopy (AFM) images of the obtained AuNPL seeds, respectively. These AuNPL seeds were fabricated as trigonal plates with a size of 154.3 ± 19.6 nm and an ∼8 nm thickness. Detailed synthesis procedures are shown in the Supporting Information. The absorption spectrum (Figure S2) shows that two resonance peaks are present at 1330 and 823 nm which are assigned to the dipolar and quadrupolar plasmon modes of AuNPLs.[37] By controlling the number of starting AuNPLs seeds in the isotropic growth, we obtained AuNPLs with gradient thicknesses of ∼15, ∼25, and ∼40 nm (Figure 1b−d). The 40 nm group also consists of a small quantity of AuNPLs with 60 nm thickness (Figure 1d). Meanwhile, according to the SEM results, the lateral dimension of these AuNPLs was increased to ∼330 nm (Figure S1b−d). The kinetic process of isotropic growth was also monitored by absorption measurements (Figure S2). As the added quantity of the starting AuNPL seeds decreases, the in-plane dipolar plasmonic peak experiences red shifts at the beginning and then changes to blue shifts. This effect corresponds to the heightened process of the AuNPLs. Specifically, the peak shows red shifts to 1380 nm for AuNPLs with an ∼15 nm thickness and then blue shifts back to 957 nm for AuNPLs with an ∼40 nm thickness. The distinct spectral shifts are due to the faster growth in the lateral rather than in the vertical direction. The heterogeneous growth rates are also reflected by the changes in their aspect ratios during the isotropic growth (Table 1). The AuNPLs with various thicknesses were mixed and serve as a TERS substrate after self-assembling a monolayer of 4NBT molecules.

**Table 1. Size, Absorption, and Aspect Ratio Evolution of AuNPLs during Isotropic Growth**

| | dipolar absorption (nm) | lateral size (nm) | thickness (nm) | aspect ratio |
|---|---|---|---|---|
| as made | 1330 | 154.3 | 8 | 19.2 |
| 1 mL of seed | 1380 | 322.3 | 15 | 21.5 |
| 0.5 mL of seed | 1180 | 336.6 | 25 | 13.5 |
| 0.2 mL of seed | 957 | 322.6 | 40 | 8.1 |

The TERS measurement was conducted in an AIST-NT-HORIBA side excitation system (45°) with a 633 nm CW laser. The laser power used throughout the TERS experiments was approximately 30 $\mu$W. TERS probes were fabricated through the metal deposition of 70 nm of Au on the Si tip (Appnano Mountain View, CA) at a 1 kHz scanning frequency. The tip-fabrication procedure is described in detail in the Supporting Information. A comparison of TERS and Raman is displayed in Figure S3, implicating that the surface enhancement of AuNPLs is not sufficient for imaging.



https://dx.doi.org/10.1021/acs.jpclett.0c01021
J. Phys. Chem. Lett. 2020, 11, 3815−3820

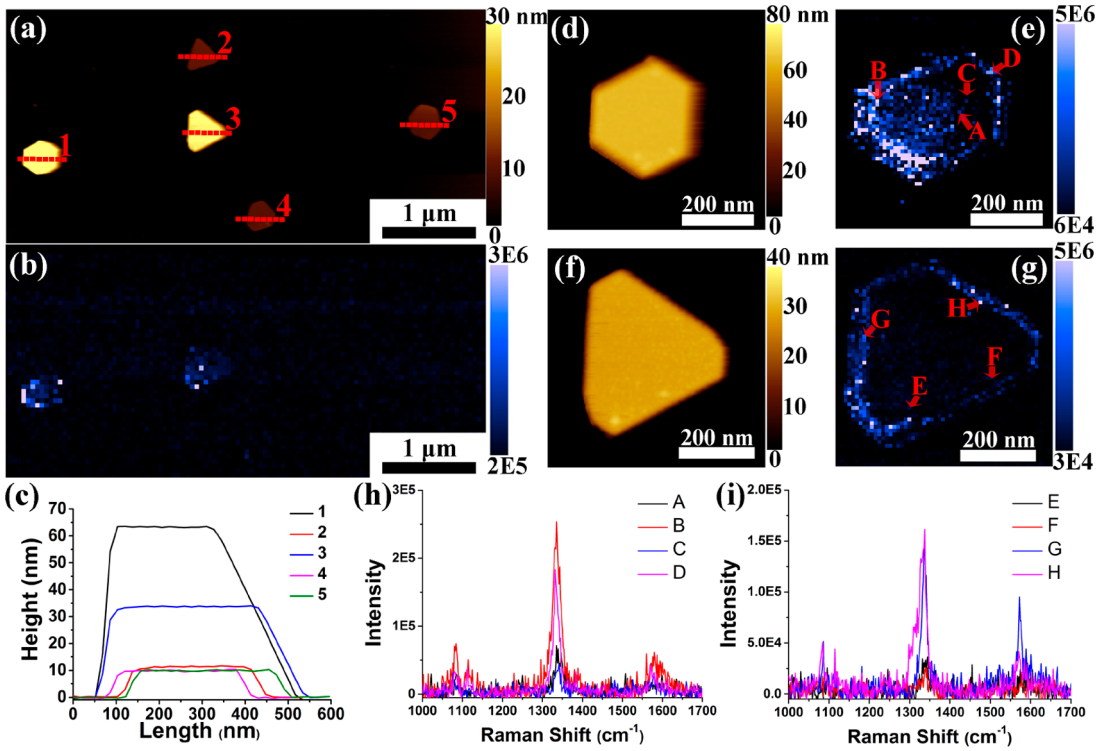


**Figure 2.** Gap-mode tip-enhanced Raman scattering with varied substrate thickness. (a) AFM and (b) TERS images of AuNPLs with thickness ranging from 10 to 65 nm. (c) Corresponding height profiles along the red dashed lines in (a). High-resolution (d, f) AFM and (e, g) TERS images of AuNPLs 1 and 3, respectively. (h, i) Typical TERS spectra extracted from the marked positions in (e) and (g), respectively. The scanning steps of (b) and (e, g) are 50 and 10 nm, respectively. The acquisition time of all of these TERS images is 200 ms.

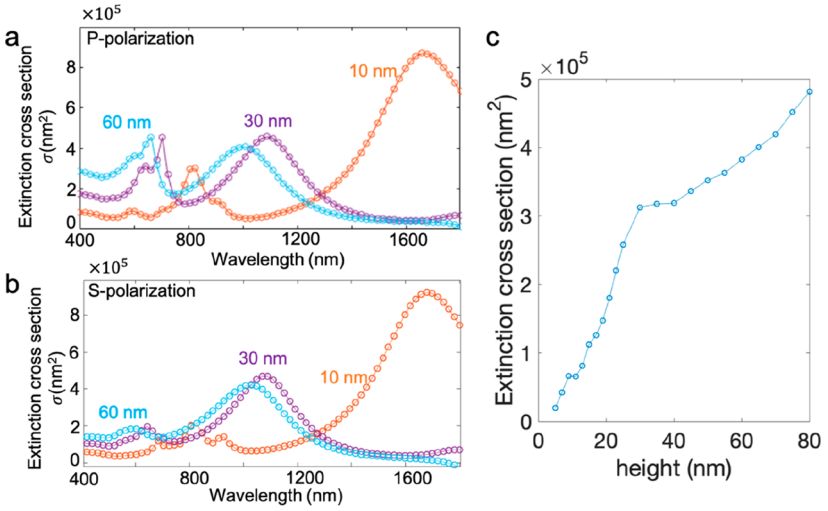


**Figure 3.** Simulated extinction cross section of the tip−AuNPL cavity by the boundary element method (BEM). (a) Localized surface plasmon resonance (LSPR) of the cavity excited by the p-polarized light. Thicker AuNPLs cause SPR blue shifts. (b) Gap plasmon excited by the s-polarized light. (c) Thickness dependence of the cross section ranging from 4 to 80 nm. The light is excited at 633 nm with p-polarization. The tip radius is 30 nm. The scale of the triangle plate is set to 400 nm.

According to the AFM image in Figure 2a, five AuNPLs (denoted as 1−5 shown in Figure 2a) with similar lateral sizes but three groups of thicknesses (i.e., 10 nm (AuNPLs 2, 4, and 5), 35 nm (AuNPL 3), and 65 nm (AuNPL 1)) were selected (Figure 2c). The isotropic characteristic has been shown in Figure S4. Instead of providing an equal enhancement, AuNPL 1 showed the highest signal intensity, followed by AuNPL 3. The TERS signals of AuNPLs 2, 4, and 5 were too noisy to be differentiated from the background. This trend is consistent with their thickness variations. Meanwhile, a similar phenomenon was also found on widely used Au microplates (Figure S5), indicating that the thickness of the substrate is a critical parameter determining enhancement factors (EFs) of gap-mode TERS.

As shown in Figure 2d−g, we obtained the high-resolution TERS images (10 nm step size) of AuNPL 1 (65 nm thickness, Figure 2d,e) and AuNPL 3 (35 nm thickness, Figure 2f,g). It should be emphasized that the edges are brighter than the


https://dx.doi.org/10.1021/acs.jpclett.0c01021
J. Phys. Chem. Lett. 2020, 11, 3815−3820

center of AuNPL in both cases, which is also confirmed by the corresponding TERS spectra (Figure 2h,i). The same phenomenon, attributed to the edge effect, has also been observed in TERS of Au microplates.[39] The edge effect, or the lightning-rod effect, is due to the concentrated charge distribution at corners or edges of micro- or nanostructures. The plasmon modes of AuNPLs are mainly excited at the edges.[40] Therefore, strong plasmonic interaction at the edge causes a gap-mode enhancement, leading to bright edges shown in Figure 2e,g and Figures S6 and S7. The TERS intensity of AuNPL 1 ranges from $5 \times 10^4$ to $3 \times 10^5$ counts, while that of AuNPL 3 ranges from $3 \times 10^4$ to $1.5 \times 10^5$ counts. On average, the signal intensity of AuNPL 1 is estimated to be approximately twice that of AuNPL 3. At the same time, the thickness of AuNPL 1 is 1.85-fold higher. The thickness of AuNPLs 2, 4, and 5 is 3.5-fold lower than that of AuNPL 3, which is comparable to twice the 1.85-fold thickness. However, their TERS signal intensities are lower than $2 \times 10^4$ counts, which is overwhelmed by the background noise. Thus, the TERS signal intensity shows a nonlinear dependence on the thickness of AuNPL. To support this hypothesis, we repeated TERS imaging on various AuNPL substrates (Figure S6). When the thickness is greater than 20 nm, the TERS signal can be sufficiently distinguished.

During the growth process, AuNPLs of hexagonal and trigonal shapes coexist. For example, in Figure 2, AuNPLs 1, 4, and 5 are closer to the hexagonal shape, and AuNPLs 2 and 3 are triangularly shaped. The hot spot distribution and extinction cross section of both forms are also shown in Figure 3 and Figures S8 and S9, implicating that their extinction cross sections are similar when the thickness is greater than 30 nm. More discussions are given in the next part to show the similar performance of both forms for TERS.

When a surface plasmon polariton (SPP) is generated along the nanoplate, charges on AuNPL accumulate at the edge, creating the bright edge hot spot. Therefore, measurements of gap-mode TERS are sensitive at the edge. The rest of the central area is bleached due to a lack of charges. AuNPLs work as nanoantennas that bring importance to the electromagnetic interaction of the tip with the AuNPL. It creates an optimal configuration for the field enhancement at the certain edge of AuNPL determined by the excitation polarization (Figure S7). As a result, a narrow edge has been observed in AuNPLs at 60−100 nm. The signal contrast of the edge and the center is shown in Figure 2h,i. The maximum counts of the nitro signal (1335 $cm^{-1}$) at the edge (B, D) and in the center (A, C) in Figure 2h are $2.5 \times 10^6$, $1.8 \times 10^6$, $7.1 \times 10^5$, and $3.9 \times 10^5$, respectively. The edge-to-center contrast can be estimated by the peak ratios of the edge and the center, which range from 2.53 to 8.33. Therefore, Figure 2h shows that though the signals with AuNPL are not homogeneous, signals along the edges are overally stronger. To compare the edges of different alignments, the same calculation was conducted for Figure 2i, which involves two bright edge spots (G, H) and two dark edge spots (E, F). Their corresponding peak intensities are $1.4 \times 10^6$, $1.6 \times 10^6$, $3.4 \times 10^5$, and $2.6 \times 10^5$. The corresponding peak ratios range from 4.11 to 6.15. The difference in the edges is attributed to their alignment against the light polarization. A detailed simulation is shown in Figure S8. Outperforming bulk Au substrates, the narrow edge effect of AuNPLs potentially leads to higher enhancement factors of TERS.

The thickness dependence can be interpreted on the basis of the gap-mode plasmon effect. The ultrasmooth AuNPL film (Figure S4) performs as a mirror-screening electric field. Therefore, an image tip can be assumed to understand the hybridized plasmonic gap. The effective coupling between the tip and an Au substrate can be approximately estimated by the tip and its mirror image on different sides of the gap.[41] This method simplifies the gap-mode model to the dual-tip configuration where the substrate is placed at the center between the tip and the mirror image. Though Au substrates are usually considered to be perfect mirrors for electric fields, with a thickness of tens of nanometers, AuNPLs cannot perform as an ideal mirror. Since thin substrates of <30 nm fail to screen the localized electric field, the image tip is distorted.[42] Under this condition, the image tip can be considered to be a partial image together with opposite charges in the far field. When the substrate becomes thicker, far-field emissions are screened, which leads to gradual changes from a partial image to a perfect mirror image. As a result, coupling of the tip and the mirror image becomes stronger; therefore, the electric field in the gap becomes more concentrated and enhanced.

In Figure 3, AuNPLs with different thicknesses are simulated via the boundary element method (BEM). The algorithm is based on the MNPBEM toolbox by Hohenester et al.[43] Detailed methods are shown in the Supporting Information. The extinction cross section is used to estimate the EF. With p-polarized incident light at 633 nm, thicker substrates show a larger cross section. Figure 3c shows the calculation of the thickness dependence. We note that the kinks in the curve of Figure 3c (extinction cross section as a function of AuNPL thickness) result from the shifting resonance peaks of Figure 3a. As the AuNPL thickness is varied, the LSPR wavelengths change, leading to nonlinear variations of the cross section for a fixed excitation wavelength. When the thicknesses of AuNPLs are 10, 30, and 60 nm, the cross sections are $6.85 \times 10^4$, $3 \times 10^5$, and $3.8 \times 10^5$ a.u., respectively. According to TERS theory, $I_{TERS} \propto \sigma|E_{inc}|^2 \times \sigma|E_{Em}|^2$, where the extinction cross section $\sigma$ is assumed to be the same for pump and Stokes wavelengths and TERS signals are proportional to $\sigma^2$. Therefore, the spectral intensity ratio of AuNPL 1 and AuNPL 3 equals 1.69. This estimation matches the measurement of peak ratio $I_{AuNPL1}/I_{AuNPL3}$ ranging from 1.67 to 2. The ratio of AuNPL 3 and AuNPL 2 is 19.18. It explains the reason that AuNPLs 2, 4, and 5 have such weak signals. Moreover, Figure 3c shows that 30 nm is a saturation thickness in improving TERS EFs. When the thickness is smaller than 30 nm, EFs are more sensitive to the thickness. As it keeps increasing, EFs will not change as much. This feature could be caused by both surface plasmon resonance and the gap-mode plasmon effect. Besides the thickness, it should be noted that the shape of the AuNPL may also play a role in the TERS enhancement. The ideal or thermodynamically stable structure of AuNPL has two {111} basal facets and six {110} side facets, making it a hexagonal appearance. However, half of {110} can grow faster than the rest in the initial growth process, making it a trigonal shape. In Figure 3 and Figure S9, we compared the extinction cross section of both shapes. When the thicknesses of the hexagonal form are 10, 30, and 60 nm, the cross sections are estimated to be $1.8 \times 10^5$, $2.6 \times 10^5$, and $4 \times 10^5$ (Figure S9). As for the trigonal case, the cross sections are $6.9 \times 10^4$, $3 \times 10^5$, and $3.8 \times 10^5$, respectively (Figure 3). When the thicknesses are 30 and 60 nm, hexagonal and trigonal forms of AuNPL have comparable cross sections. When the thickness is less than 30 nm, as we hardly observed TERS signals with


https://dx.doi.org/10.1021/acs.jpclett.0c01021
J. Phys. Chem. Lett. 2020, 11, 3815−3820

either form, their difference in Raman enhancements are not concerned. In the case of 633 nm excitation, according to our simulation, TERS might be affected by both the shape and thickness of AuNPL when the thickness is below 30 nm but will be solely affected by the thickness when it is greater than 30 nm.

One of the most concerning artifacts in TERS imaging is tip contamination. In some independent cases, we also witnessed this alternative mechanism and found that it was distinct from our previous results. As shown in Figure S10a, the signals spread over the last several lines of the scanning. Positions such as 3 and 4 also show strong characteristic signals of 4-NBT even if no AuNPL is expected (Figure S10c). These results indicate that the tip was contaminated by picking up thiolate molecules during TERS mapping. The tip contamination is an unpredictable issue before TERS mapping and can make a tip blunt and unstable and always causes obscure images instead of the high-resolution ones presented in Figure 2. Therefore, the TERS images in this letter demonstrates that they are not caused by tip contamination.

We performed a detailed spectroscopic investigation on the gap-mode TERS using AuNPLs as substrates. Because of the edge effect, AuNPLs display a nonuniform hot spot distribution. The interaction of hot spots and the tip results in the further improvement of TERS sensitivity. Besides, it is found that the TERS signal intensity shows a positive correlation with AuNPL thickness. Moreover, both experimentally and theoretically, we confirmed a saturation thickness of 30 nm for gap-mode TERS and assumed that a well-grown AuNPL substrate at 30 nm can sufficiently facilitate TERS measurement with high sensitivity.

## ■ ASSOCIATED CONTENT

### Supporting Information

The Supporting Information is available free of charge at https://pubs.acs.org/doi/10.1021/acs.jpclett.0c01021.

Synthesis of AuNPLs; preparation of a 4NBT monolayer on AuNPL; TERS probes fabrication; TERS measurement parameters; BEM modeling details; SEM images and the absorption of AuNPLs; TERS of Au microplates; and BEM modeling results of AuNPLs (PDF)

## ■ AUTHOR INFORMATION


### Corresponding Author

**Dmitry Kurouski** − *Department of Biochemistry and Biophysics and The Institute for Quantum Science and Engineering, Texas A&M University, College Station, Texas 77843, United States;* orcid.org/0000-0002-6040-4213; Email: dkurouski@tamu.edu

### Authors

**Rui Wang** − *Department of Biochemistry and Biophysics, Texas A&M University, College Station, Texas 77843, United States;* orcid.org/0000-0002-9452-9241

**Zhe He** − *Department of Physics, Texas A&M University, College Station, Texas 77843, United States;* orcid.org/0000-0002-8525-3650

**Alexei V. Sokolov** − *Department of Physics and The Institute for Quantum Science and Engineering, Texas A&M University, College Station, Texas 77843, United States*

Complete contact information is available at: https://pubs.acs.org/10.1021/acs.jpclett.0c01021

### Author Contributions

‖R.W. and Z.H. contributed equally to this work.


### Notes

The authors declare no competing financial interest.

## ■ ACKNOWLEDGMENTS

R.W. and Z.H. conceived and performed the experiment. D.K. developed and hosted the laboratory. R.W. produced the AuNPL sample. Z.H. developed the model and did the simulations. R.W., Z.H., A.V.S., and D.K. discussed and wrote the manuscript. All authors contributed to the experiments and manuscript preparation. This work was supported by the Office of Naval Research (grant no. N00014-16-1-2578) and the Robert A. Welch Foundation (grant No. A-1547). Z.H. was supported by the Herman F. Heep and Minnie Belle Heep Texas A&M University Endowed Fund held and administered by the Texas A&M Foundation.

## ■ REFERENCES


(1) Liu, J.; Yu, M.; Zhou, C.; Yang, S.; Ning, X.; Zheng, J. Passive Tumor Targeting of Renal-Clearable Luminescent Gold Nanoparticles: Long Tumor Retention and Fast Normal Tissue Clearance. *J. Am. Chem. Soc.* **2013**, *135*, 4978−4981.

(2) Liu, C.-L.; Ho, M.-L.; Chen, Y.-C.; Hsieh, C.-C.; Lin, Y.-C.; Wang, Y.-H.; Yang, M.-J.; Duan, H.-S.; Chen, B.-S.; Lee, J.-F. Thiol-Functionalized Gold Nanodots: Two-Photon Absorption Property and Imaging in Vitro. *J. Phys. Chem. C* **2009**, *113*, 21082−21089.

(3) Zavaleta, C. L.; Smith, B. R.; Walton, I.; Doering, W.; Davis, G.; Shojaei, B.; Natan, M. J.; Gambhir, S. S. Multiplexed Imaging of Surface Enhanced Raman Scattering Nanotags in Living Mice Using Noninvasive Raman Spectroscopy. *Proc. Natl. Acad. Sci. U. S. A.* **2009**, *106*, 13511−13516.

(4) Yang, J.; Shen, D.; Zhou, L.; Li, W.; Li, X.; Yao, C.; Wang, R.; El-Toni, A. M.; Zhang, F.; Zhao, D. Spatially Confined Fabrication of Core−Shell Gold Nanocages@ Mesoporous Silica for near-Infrared Controlled Photothermal Drug Release. *Chem. Mater.* **2013**, *25*, 3030−3037.

(5) Wang, R.; Zhou, L.; Wang, W.; Li, X.; Zhang, F. In Vivo Gastrointestinal Drug-Release Monitoring through Second near-Infrared Window Fluorescent Bioimaging with Orally Delivered Microcarriers. *Nat. Commun.* **2017**, *8*, 14702.

(6) Li, X.; Zhao, T.; Lu, Y.; Wang, P.; El-Toni, A. M.; Zhang, F.; Zhao, D. Degradation-Restructuring Induced Anisotropic Epitaxial Growth for Fabrication of Asymmetric Diblock and Triblock Mesoporous Nanocomposites. *Adv. Mater.* **2017**, *29*, 1701652.

(7) Dai, Q.; Ouyang, M.; Yuan, W.; Li, J.; Guo, B.; Lan, S.; Liu, S.; Zhang, Q.; Lu, G.; Tie, S. Encoding Random Hot Spots of a Volume Gold Nanorod Assembly for Ultralow Energy Memory. *Adv. Mater.* **2017**, *29*, 1701918.

(8) Ben-Shahar, Y.; Philbin, J. P.; Scotognella, F.; Ganzer, L.; Cerullo, G.; Rabani, E.; Banin, U. Charge Carrier Dynamics in Photocatalytic Hybrid Semiconductor−Metal Nanorods: Crossover from Auger Recombination to Charge Transfer. *Nano Lett.* **2018**, *18*, 5211−5216.

(9) Liu, P.; Qin, R.; Fu, G.; Zheng, N. Surface Coordination Chemistry of Metal Nanomaterials. *J. Am. Chem. Soc.* **2017**, *139*, 2122−2131.

(10) Zhu, X.; Jia, H.; Zhu, X. M.; Cheng, S.; Zhuo, X.; Qin, F.; Yang, Z.; Wang, J. Selective Pd Deposition on Au Nanobipyramids and Pd Site-Dependent Plasmonic Photocatalytic Activity. *Adv. Funct. Mater.* **2017**, *27*, 1700016.

(11) Jeanmaire, D. L.; Van Duyne, R. P. Surface Raman Spectroelectrochemistry: Part I. Heterocyclic, Aromatic, and Aliphatic Amines Adsorbed on the Anodized Silver Electrode. *J. Electroanal. Chem. Interfacial Electrochem.* **1977**, *84*, 1−20.

(12) Albrecht, M. G.; Creighton, J. A. Anomalously Intense Raman Spectra of Pyridine at a Silver Electrode. *J. Am. Chem. Soc.* **1977**, *99*, 5215−5217.
(13) Moskovits, M. Surface Roughness and the Enhanced Intensity of Raman Scattering by Molecules Adsorbed on Metals. *J. Chem. Phys.* **1978**, *69*, 4159−4161.
(14) Zheng, X.; Zong, C.; Xu, M.; Wang, X.; Ren, B. Raman Imaging from Microscopy to Nanoscopy, and to Macroscopy. *Small* **2015**, *11*, 3395−3406.
(15) Hapala, P.; Kichin, G.; Wagner, C.; Tautz, F. S.; Temirov, R.; Jelínek, P. Mechanism of High-Resolution Stm/Afm Imaging with Functionalized Tips. *Phys. Rev. B: Condens. Matter Mater. Phys.* **2014**, *90*, 085421.
(16) de la Torre, B.; Švec, M.; Foti, G.; Krejčí, O.; Hapala, P.; Garcia-Lekue, A.; Frederiksen, T.; Zbořil, R.; Arnau, A.; Vázquez, H. Submolecular Resolution by Variation of the Inelastic Electron Tunneling Spectroscopy Amplitude and Its Relation to the Afm/Stm Signal. *Phys. Rev. Lett.* **2017**, *119*, 166001.
(17) Stöckle, R. M.; Suh, Y. D.; Deckert, V.; Zenobi, R. Nanoscale Chemical Analysis by Tip-Enhanced Raman Spectroscopy. *Chem. Phys. Lett.* **2000**, *318*, 131−136.
(18) Stadler, J.; Schmid, T.; Zenobi, R. Nanoscale Chemical Imaging Using Top-Illumination Tip-Enhanced Raman Spectroscopy. *Nano Lett.* **2010**, *10*, 4514−4520.
(19) Zhang, R.; Zhang, Y.; Dong, Z.; Jiang, S.; Zhang, C.; Chen, L.; Zhang, L.; Liao, Y.; Aizpurua, J.; Luo, Y. e. Chemical Mapping of a Single Molecule by Plasmon-Enhanced Raman Scattering. *Nature* **2013**, *498*, 82−86.
(20) He, Z.; et al. Tip-Enhanced Raman Imaging of Single-Stranded DNA with Single Base Resolution. *J. Am. Chem. Soc.* **2019**, *141*, 753−757.
(21) Lee, J.; Crampton, K. T.; Tallarida, N.; Apkarian, V. A. Visualizing Vibrational Normal Modes of a Single Molecule with Atomically Confined Light. *Nature* **2019**, *568*, 78−82.
(22) Jiang, S.; Zhang, Y.; Zhang, R.; Hu, C.; Liao, M.; Luo, Y.; Yang, J.; Dong, Z.; Hou, J. G. Distinguishing Adjacent Molecules on a Surface Using Plasmon-Enhanced Raman Scattering. *Nat. Nanotechnol.* **2015**, *10*, 865−869.
(23) Yang, Z.; Aizpurua, J.; Xu, H. Electromagnetic Field Enhancement in Ters Configurations. *J. Raman Spectrosc.* **2009**, *40*, 1343−1348.
(24) Deckert-Gaudig, T.; Deckert, V. Ultraflat Transparent Gold Nanoplates—Ideal Substrates for Tip-Enhanced Raman Scattering Experiments. *Small* **2009**, *5*, 432−436.
(25) Marr, J. M.; Schultz, Z. D. Imaging Electric Fields in Sers and Ters Using the Vibrational Stark Effect. *J. Phys. Chem. Lett.* **2013**, *4*, 3268−3272.
(26) Sonntag, M. D.; Klingsporn, J. M.; Garibay, L.; Roberts, J. M.; Dieringer, J. A.; Seideman, T.; Scheidt, K. A.; Jensen, L.; Schatz, G. C.; Van Duyne, R. P. Single-Molecule Tip-Enhanced Raman Spectroscopy. *J. Phys. Chem. C* **2012**, *116*, 478−483.
(27) Bhattarai, A.; Crampton, K. T.; Joly, A. G.; Kovarik, L.; Hess, W. P.; El-Khoury, P. Z. Imaging the Optical Fields of Functionalized Silver Nanowires through Molecular Ters. *J. Phys. Chem. Lett.* **2018**, *9*, 7105−7109.
(28) Bhattarai, A.; Novikova, I. V.; El-Khoury, P. Z. Tip-Enhanced Raman Nanographs of Plasmonic Silver Nanoparticles. *J. Phys. Chem. C* **2019**, *123*, 27765−27769.
(29) Wang, R.; Kurouski, D. Elucidation of Tip-Broadening Effect in Tip-Enhanced Raman Spectroscopy (Ters): A Cause of Artifacts or Potential for 3d Ters. *J. Phys. Chem. C* **2018**, *122*, 24334−24340.
(30) Wang, R.; Li, J.; Rigor, J.; Large, N.; El-Khoury, P.; Yu, R. A.; Kurouski, D. Direct Experimental Evidence of Hot-Carrier-Driven Chemical Processes in Tip-Enhanced Raman Spectroscopy (Ters). *J. Phys. Chem. C* **2020**, *124*, 2238−2244.
(31) Li, G.-C.; Zhang, Q.; Maier, S. A.; Lei, D. Plasmonic Particle-on-Film Nanocavities: A Versatile Platform for Plasmon-Enhanced Spectroscopy and Photochemistry. *Nanophotonics* **2018**, *7*, 1865−1889.
(32) Chen, L.; Ji, F.; Xu, Y.; He, L.; Mi, Y.; Bao, F.; Sun, B.; Zhang, X.; Zhang, Q. High-Yield Seedless Synthesis of Triangular Gold Nanoplates through Oxidative Etching. *Nano Lett.* **2014**, *14*, 7201−7206.
(33) Qin, F.; Zhao, T.; Jiang, R.; Jiang, N.; Ruan, Q.; Wang, J.; Sun, L.-D.; Yan, C.-H.; Lin, H.-Q. Thickness Control Produces Gold Nanoplates with Their Plasmon in the Visible and near-Infrared Regions. *Adv. Opt. Mater.* **2016**, *4*, 76−85.
(34) Garcia-Rico, E.; Alvarez-Puebla, R. A.; Guerrini, L. Direct Surface-Enhanced Raman Scattering (Sers) Spectroscopy of Nucleic Acids: From Fundamental Studies to Real-Life Applications. *Chem. Soc. Rev.* **2018**, *47*, 4909−4923.
(35) van Schrojenstein Lantman, E. M.; Deckert-Gaudig, T.; Mank, A. J.; Deckert, V.; Weckhuysen, B. M. Catalytic Processes Monitored at the Nanoscale with Tip-Enhanced Raman Spectroscopy. *Nat. Nanotechnol.* **2012**, *7*, 583.
(36) Scarabelli, L.; Coronado-Puchau, M.; Giner-Casares, J. J.; Langer, J.; Liz-Marzán, L. M. Monodisperse Gold Nanotriangles: Size Control, Large-Scale Self-Assembly, and Performance in Surface-Enhanced Raman Scattering. *ACS Nano* **2014**, *8*, 5833−5842.
(37) Millstone, J. E.; Park, S.; Shuford, K. L.; Qin, L.; Schatz, G. C.; Mirkin, C. A. Observation of a Quadrupole Plasmon Mode for a Colloidal Solution of Gold Nanoprisms. *J. Am. Chem. Soc.* **2005**, *127*, 5312−5313.
(38) Huang, Y.; Ferhan, A. R.; Gao, Y.; Dandapat, A.; Kim, D.-H. High-Yield Synthesis of Triangular Gold Nanoplates with Improved Shape Uniformity, Tunable Edge Length and Thickness. *Nanoscale* **2014**, *6*, 6496−6500.
(39) Bhattarai, A.; Joly, A. G.; Krayev, A.; El-Khoury, P. Z. Taking the Plunge: Nanoscale Chemical Imaging of Functionalized Gold Triangles in H2o Via Ters. *J. Phys. Chem. C* **2019**, *123*, 7376−7380.
(40) Xu, X.-b.; Luo, J.-s.; Liu, M.; Wang, Y.-y.; Yi, Z.; Li, X.-b.; Yi, Y.-g.; Tang, Y.-j. The Influence of Edge and Corner Evolution on Plasmon Properties and Resonant Edge Effect in Gold Nanoplatelets. *Phys. Chem. Chem. Phys.* **2015**, *17*, 2641−2650.
(41) Li, A.; Isaacs, S.; Abdulhalim, I.; Li, S. Ultrahigh Enhancement of Electromagnetic Fields by Exciting Localized with Extended Surface Plasmons. *J. Phys. Chem. C* **2015**, *119*, 19382−19389.
(42) Tsai, F.-C.; Weng, C.-H.; Chen, Y. L.; Shih, W.-P.; Chang, P.-Z. Color Rendering Based on a Plasmon Fullerene Cavity. *Opt. Express* **2018**, *26*, 9984−9999.
(43) Hohenester, U.; Trügler, A. Mnpbem−a Matlab Toolbox for the Simulation of Plasmonic Nanoparticles. *Comput. Phys. Commun.* **2012**, *183*, 370−381.


https://dx.doi.org/10.1021/acs.jpclett.0c01021
J. Phys. Chem. Lett. 2020, 11, 3815−3820